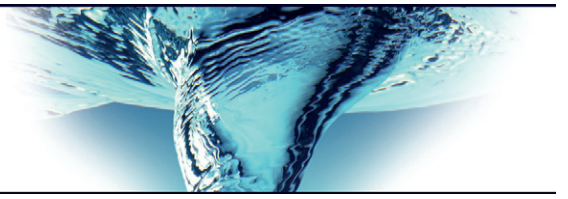
CrossMark

J. Fluid Mech. (2017), *vol.* 820, R3, doi:10.1017/jfm.2017.245



JFM RAPIDS
journals.cambridge.org/rapids

Fractal scaling of the turbulence interface in gravity currents

Dominik Krug[1,†], Markus Holzner[2], Ivan Marusic[1] and Maarten van Reeuwijk[3]

[1]Department of Mechanical Engineering, University of Melbourne, Victoria 3010, Australia

[2]Institute of Environmental Engineering, ETH Zürich, CH-8039 Zürich, Switzerland

[3]Department of Civil and Environmental Engineering, Imperial College London, SW7 2AZ London, UK

(Received 23 January 2017; revised 11 April 2017; accepted 11 April 2017; first published online 9 May 2017)

It was previously observed by Krug *et al.* (*J. Fluid Mech.*, vol. 765, 2015, pp. 303–324) that the surface area A_η of the turbulent/non-turbulent interface (TNTI) in gravity currents decreases with increasing stratification, significantly reducing the entrainment rate. Here, we consider the multiscale properties of this effect using direct numerical simulations of temporal gravity currents with different gradient Richardson numbers Ri_g. Our results indicate that the reduction of A_η is caused by a decrease of the fractal scaling exponent β, while the scaling range remains largely unaffected. We further find that convolutions of the TNTI are characterized by different length scales in the streamwise and wall-normal directions, namely the integral scale h and the shear scale $l_{Sk} = k^{1/2}/S$ (formed using the mean shear S and the turbulent kinetic energy k) respectively. By recognizing that the anisotropy implied by the different scaling relations increases with increasing Ri_g, we are able to model the Ri_g dependence of β in good agreement with the data.

Key words: geophysical and geological flows, gravity currents, stratified turbulence

1. Introduction

It has long been established that in partially or fully unconfined turbulent flows, such as jets, wakes and boundary layers, regions of turbulent and non-turbulent flow are separated by sharp and strongly contorted interfaces (e.g. Corrsin & Kistler 1954; Da Silva *et al.* 2014). Interest in these turbulent/non-turbulent interfaces (TNTIs) has remained high since they play a crucial role in setting the entrainment rate, which is

† Email address for correspondence: dkrug@unimelb.edu.au

© Cambridge University Press 2017

https://doi.org/10.1017/jfm.2017.245 Published online by Cambridge University Press

an important parameter in many practical applications. In particular, when following the conventional approach of defining the instantaneous TNTI using an appropriate threshold on enstrophy ω^2, where ω denotes the norm of the vorticity vector, a local entrainment velocity describing the motion of the TNTI relative to the fluid can be computed from $v_n \equiv -|\nabla\omega^2|^{-1}\,\mathrm{D}\omega^2/\mathrm{D}t$ (Holzner & Lüthi 2011). The entrained volume flux is then given by the surface integral

$$Q_\omega \equiv \int_{A_\eta} v_n \,\mathrm{d}A = \langle v_n \rangle A_\eta, \tag{1.1}$$

where $\langle\cdot\rangle$ denotes an average over the surface area of the TNTI, A_η. While v_n is widely observed to be of the order of the small-scale (Kolmogorov) velocity u_η (Holzner & Lüthi 2011), the multiscale aspect of turbulent entrainment is reflected in A_η, which is set by eddies distorting the TNTI across the full range of scales.

The flow case under consideration here is a gravity current originating from a continuous release of heavier fluid along a sloping bottom into uniform surroundings. This problem was originally investigated by Ellison & Turner (1959), who found that the entrainment parameter E is a decreasing function of the Richardson number, Ri, which represents the ratio of the competing forces of stratification and shear (see § 3 for exact definitions). A sound understanding of how E varies depending on the flow parameters is important, e.g., in the study of turbidity currents, where surprisingly high runout lengths have been linked to very low entrainment rates (Sequeiros *et al.* 2010; Sequeiros 2012; Kneller *et al.* 2016). In a recent effort to elucidate this behaviour of E in relation to properties of the TNTI, Krug *et al.* (2015) showed that the reduction of E is in significant part due to a decrease of A_η with increasing Ri, whereas $\langle v_n \rangle/u_\eta$ remains largely unaffected. Their experimental findings have since been confirmed by the direct numerical simulations (DNS) of van Reeuwijk, Krug & Holzner (2017). A key to understanding the entrainment rate in gravity currents – and quite possibly also to modelling it – therefore lies in understanding the behaviour of A_η. Hence, the goal of the present study is to investigate stratification effects on A_η using a multiscale approach. The analytical tools necessary are available from numerous related studies on flows without a stable density stratification, which are summarized in the review of Sreenivasan (1991). Their most relevant result is the prediction of fractal scaling in the inertial region based on the proposal of scale invariance for turbulent geometries by Mandelbrot (1982). Fractal scaling for the TNTI implies power-law behaviour according to Sreenivasan, Ramshankar & Meneveau (1989),

$$A_\eta = A_0 (l_i/l_o)^{2-D_f}, \tag{1.2}$$

where l_i and l_o are the inner and outer cutoffs of the inertial scaling range respectively. Theoretical predictions yield $D_f = 7/3$ for the fractal dimension, in good agreement with recent high-Reynolds-number (Re) experiments by de Silva *et al.* (2013), who find $D_f \approx 2.3$–2.4 for the TNTI in turbulent boundary layers. It should be noted that others (e.g. Dimotakis & Catrakis 1999) argue that D_f should be scale-dependent. However, a significant scale separation is required to address this issue, and this will not be the focus here. The goal of the present study is to ascertain how the previously observed decrease of A_η/A_0 with increasing Ri is reflected in changes of the fractal scaling parameters l_i, l_o and D_f compared with the unstratified case where $Ri = 0$. To this end, we make use of DNS of a temporal version of the gravity current problem previously introduced in van Reeuwijk *et al.* (2017). Before presenting our results in § 3 followed by a discussion in § 4, details of the simulations are given in § 2. Our conclusions are summarized in § 5.

https://doi.org/10.1017/jfm.2017.245 Published online by Cambridge University Press

Label	α (deg.)	Ri_0	Re_0	$\hat{Re}_\lambda = \sqrt{15/(\nu\hat{\varepsilon})}\hat{k}$	$N_x N_y N_z$	$L_x L_y L_z / h_0^3$
GC1	20	0.04	3700	141	$1536^2 \times 1152$	$20^2 \times 10$
GC2	10	0.11	3700	107	$1536^2 \times 1152$	$20^2 \times 10$
GC3	5	0.22	3700	72	$1536^2 \times 1152$	$20^2 \times 10$
WJ	—	0	3700	115	$1536^2 \times 1152$	$20^2 \times 10$

TABLE 1. Simulation parameters: N_i and L_i denote the number of grid points and the domain size along the i-direction respectively; subscript '0' marks quantities at the start of the simulation. Results for $\hat{Re}_\lambda$ are averaged over $100 < \tilde{t} < 120$.

2. Simulations

In the temporal gravity current simulated here, the flow evolves in time (instead of along the streamwise coordinate as in the spatial case) due to periodic boundary conditions not only in the spanwise but also in the streamwise direction. A detailed discussion of the concept and the numerical configuration used was recently provided in van Reeuwijk *et al.* (2017), who also confirmed that the aforementioned findings of Krug *et al.* (2015) transfer to the temporal problem. The simulations presented here were carried out using a fourth-order accurate discretization of the Navier–Stokes equations in the Boussinesq approximation (Craske & van Reeuwijk 2015). The flow is initialized with uniform distributions of streamwise velocity u_0 and buoyancy b_0 up to a height h_0 above the bottom wall (located at $z = 0$), and is statistically homogeneous in the streamwise (x) and spanwise (y) directions. The buoyancy vector is given by $\boldsymbol{b} = b\hat{\boldsymbol{g}}$, where b is a scalar with Schmidt number $Sc = 1$ and the unit vector $\hat{\boldsymbol{g}}$ is tilted at an angle α with respect to the vertical (i.e. the z axis) in order to simulate a sloping bottom. Hence, the component $b\sin(\alpha)$ drives the flow along x, while $b\cos(\alpha)$ is causing a stable stratification in the wall-normal direction. Throughout this paper, we make use of the top-hat definitions

$$u_T h = \int_0^\infty \overline{u}\,\mathrm{d}z, \quad u_T^2 h = \int_0^\infty \overline{u}^2\,\mathrm{d}z \quad \text{and} \quad b_T h = \int_0^\infty \overline{b}\,\mathrm{d}z = B_0, \tag{2.1a–c}$$

where u is the streamwise velocity (the overline indicates averaging in wall-parallel planes; the corresponding fluctuations are given by $u' = u - \overline{u}$) and the buoyancy content B_0 is a conserved quantity in the temporal problem (van Reeuwijk *et al.* 2017). The velocity components along the y- and z-axes are denoted by v and w respectively. With the above definitions, we can form a bulk Reynolds number $Re = u_T h/\nu$, where ν is the kinematic viscosity, and a Richardson number $Ri = B_0\cos(\alpha)/u_T^2$. Table 1 summarizes the parameters of the simulations employed in this study. For the gravity currents (labelled GCs in the following), Ri_0 is varied by changing the inclination angle α while keeping the integral forcing $\sin(\alpha)B_0$ in the x-direction constant. In addition, we ran a simulation with the buoyancy term switched off, resulting in an unstratified (temporal) wall jet (WJ) that is driven by initial momentum only. Apart from the bulk flow behaviour, where the whole domain was used, results will be based on averages over six independent xz-planes, which are spaced equally in the y-direction, amounting to 250 snapshots over a period of 120 h_0/u_0.

https://doi.org/10.1017/jfm.2017.245 Published online by Cambridge University Press

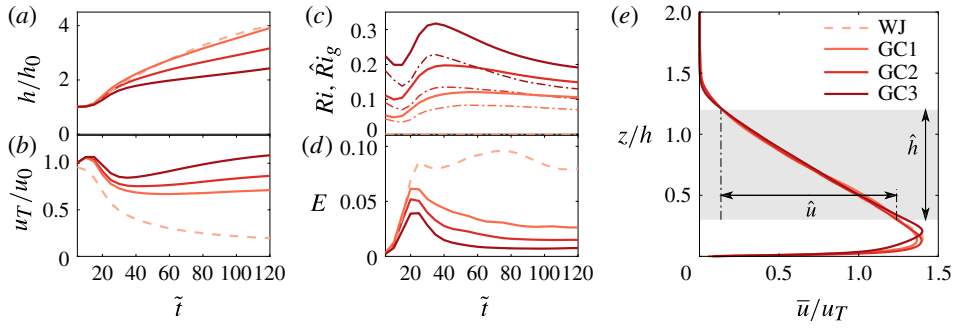


FIGURE 1. Temporal evolution of (*a*) top-hat thickness h, (*b*) top-hat velocity u_T, (*c*) Ri (thick) and Ri_g (dashed-dotted lines) and (*d*) entrainment coefficient E. (*e*) Mean profiles of streamwise velocity at $\tilde{t} = 100$, with the grey shading indicating the averaging band for turbulence quantities. The legend in (*e*) applies to all panels; the colour scheme is chosen such that darker shades of red correspond to larger Ri.

3. Results

The bulk flow behaviour in terms of h and u_T is presented in figure 1 as a function of the dimensionless time $\tilde{t} = tu_0/h_0$. After an initial transient, these quantities are observed to evolve conforming to their inviscid scaling $h \propto \tilde{t}$ and $u_T \propto$ const. for GCs, and $h \propto \tilde{t}^{1/2}$ and $u_T \propto \tilde{t}^{-1/2}$ for the WJ (van Reeuwijk *et al.* 2017), with a clear trend of decreasing h and increasing u_T with increasing Ri_0. As figure 1(*c*) shows, Ri asymptotes towards different constants for $\tilde{t} \gtrsim 90$ for the GC simulations. In accordance with previous findings, this relates also to different values of the entrainment parameter E shown in figure 1(*d*), which is defined as $E = u_T^{-1}\,\mathrm{d}h/\mathrm{d}t$ for temporal flows. In equilibrium flow, both $Ri \to$ const. and $E \to$ const., such that figure 1(*c*,*d*) provides further indicators that equilibrium has indeed been reached in the simulations. We further note that E for all GCs is significantly reduced compared with the WJ, for which $Ri = 0$ at all times.

The basic structure of the flow can be inferred from the profiles of $\overline{u}$ displayed in figure 1(*e*). Starting from the wall where $\overline{u} = 0$, the velocity increases sharply within the boundary layer up to a maximum at $z/h \approx 0.15$, followed by a decrease back to zero at $z/h \approx 1.5$. In the region $0.3 < z/h < 1.2$, this decrease – and similarly the one for $\overline{b}$ (not shown) – is linear to a very good approximation. In order to exclude the influence of the near-wall region, where wall scaling prevails, from entering the statistics, we will restrict averages to this region in the following and denote this by using $\hat{(\cdot)}$. As indicated in the figure, $\hat{h} = 0.9h$ and $\hat{u} \approx 1.1u_T$, and we define the gradient Richardson number as $\hat{Ri}_g = (\hat{N}/\hat{S})^2$, where $\hat{N}^2 = \mathrm{d}\overline{b}/\mathrm{d}z$ is the buoyancy frequency and $\hat{S} = \mathrm{d}\overline{u}/\mathrm{d}z$ is the shear. Results for $\hat{Ri}_g$ are also included in figure 1(*c*) (dashed-dotted lines), and it is obvious that the behaviour resembles that of Ri with slightly lower magnitudes. Furthermore, we point out that even though there are fundamental differences between the WJ and the GCs, the collapse in figure 1(*e*) indicates that the structures of the flows are indeed very similar.

The position of the TNTI is detected using a threshold on the enstrophy $\omega^2 = \omega_i\omega_i$, where ω_i is the vorticity vector. For simplicity, a single threshold value $\omega^2_{thr} = 3 \times 10^{-5}u_0^2/h_0^2$ is chosen here at all times and for all flows. Two sample ω^2-snapshots in figure 2(*a*,*b*) for WJ and GC2 provide evidence for the suitability of this criterion.

https://doi.org/10.1017/jfm.2017.245 Published online by Cambridge University Press

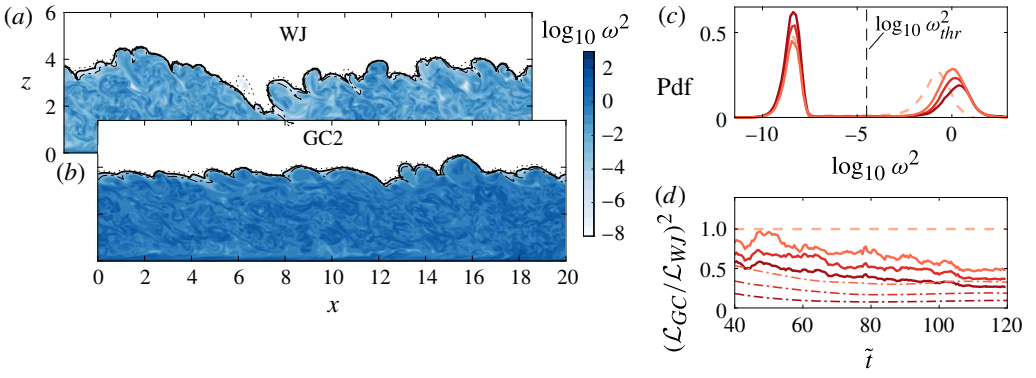


FIGURE 2. Snapshots of the enstrophy distribution in (*a*) WJ at $\tilde{t}=60$ and (*b*) GC2 at $\tilde{t}=90$, with the times selected such that $h=2.75$ in both flows. Black solid lines indicate the position of the TNTI along with isocontours at $100\omega_{thr}^2$ (dash-dotted) and $0.01\omega_{thr}^2$ (dotted). (*c*) Probability density function (p.d.f.) of $\log_{10}\omega^2$ at $\tilde{t}=120$ and (*d*) squared ratio of interface lengths $(\mathcal{L}_{GC}/\mathcal{L}_{WJ})^2$ (thick lines) along with E_{GC}/E_{WJ} (dash-dotted lines). The legend from figure 1(*e*) applies.

These figures further demonstrate that the location of the TNTI hardly changes even when varying the threshold value over a range of four orders of magnitude in total. Consequently, the results presented in the following are also largely independent of the exact choice of ω_{thr}^2. Further, figure 2(*c*) presents a probability density function of $\log_{10}\omega^2$ at the end of the simulations, when the differences between the flows are maximal. The distribution is bimodal, with the peaks corresponding to the turbulent region (high ω^2) and an essentially irrotational region (low ω^2). From this figure, it is clear that the threshold is suitably chosen to differentiate between the two regions.

As a next step, we focus on the multiscale properties of the interface. For the ease of data handling and computation, instead of considering A_η itself, we will consider its 2D surrogate in the following, which corresponds to the length $\mathcal{L}$ of the TNTI contours in snapshots such as those shown in figure 2(*a*,*b*). These snapshots were chosen such that h is nominally the same, and it is obvious that in this case $\mathcal{L}_{WJ}$ is significantly larger than $\mathcal{L}_{GC2}$. In order to relate results from xz-snapshots to A_η, it has to be assumed that interface convolutions in the yz-plane are similar, which has been shown to be valid for wall jets (Paizis & Schwarz 1974). Accordingly, we plot $(\mathcal{L}_{GC}/\mathcal{L}_{WJ})^2$ as a surrogate for $A_{\eta,GC}/A_{\eta,WJ}$ in figure 2(*d*). We note that this ratio reaches values as low as 0.5, which is of the order of the relative reduction in E also plotted in the figure. This observation again emphasizes the important role the reduction of A_η plays in reducing E.

Since the quantity of interest here is the length $\mathcal{L}$ at different scales, we investigate the fractal scaling of the TNTI based on filtered fields similarly to de Silva *et al.* (2013). Before filtering, we transform ω^2 to the binary field I, where $I=1$ if $\omega^2 \geqslant \omega_{thr}^2$ and $I=0$ otherwise. As illustrated in figure 3, this field is then filtered according to $\tilde{I}=\int I(\boldsymbol{x}-\boldsymbol{x}')G(\boldsymbol{x}')\,\mathrm{d}^2\boldsymbol{x}'$, with G denoting the kernel of a square box-filter with filter width λ. In the filtered fields, the TNTI is then found where $\tilde{I}=0.5$. The main advantage of this procedure as opposed to filtering ω^2 directly is that it approximately preserves the mean interface position. Based on a self-similarity argument (van Reeuwijk & Holzner 2014), this is a prerequisite to expecting fluxes across the TNTI evaluated at different scales to be equal, i.e. $Q_\omega(\lambda)=Q_\omega$.

https://doi.org/10.1017/jfm.2017.245 Published online by Cambridge University Press

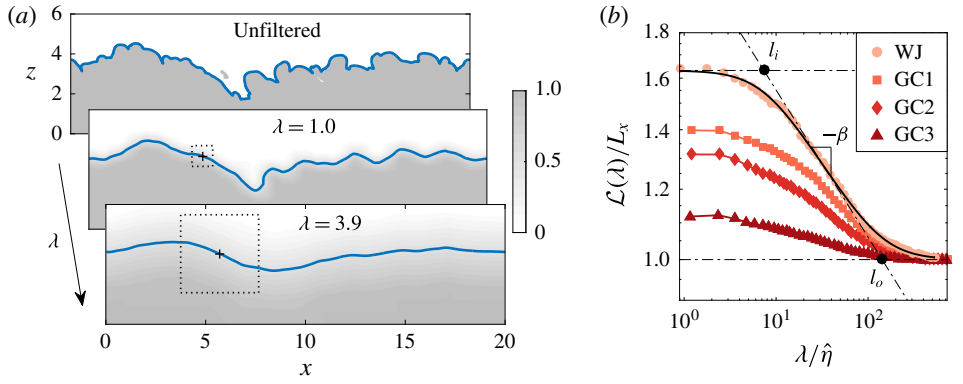


FIGURE 3. (*a*) Illustration of the filtering procedure applied to the ω^2-snapshot shown in figure 2(*a*). The blue line represents the TNTI at the respective filter scale. (*b*) Interface length $\mathcal{L}(\lambda)$ at $\tilde{t} = 60$ for all simulations. The black solid line corresponds to the fit for WJ according to (3.1).

The equivalent of (1.2) for $\mathcal{L}$ evaluated at a filter scale is given by $\mathcal{L}(\lambda) \propto \lambda^{-\beta}$, where $\beta \approx 0.3$–0.4 (de Silva *et al.* 2013). Sample results for $\mathcal{L}(\lambda)$ are depicted in figure 3(*b*), where λ is normalized by the Kolmogorov scale $\hat{\eta} = (\nu^3/\hat{\varepsilon})^{1/4}$ and $\hat{\varepsilon}$ is the rate of turbulent dissipation. The curves level off at small and large λ, which relate to the outer and inner cutoffs respectively. However, the transitions are smooth, such that the determination of l_i and l_o is not straightforward. Given the limited range of scales in the simulation, the slope β will also vary depending on the chosen scaling range. To determine the fractal scaling parameters nevertheless in a consistent and unambiguous manner, despite the moderate Re, we make use of the fit function

$$\frac{\mathcal{L}(\lambda)}{L_x} = \left(\frac{l_o}{l_i}\right)^{\beta} \left[\frac{1 + (\lambda/l_o)^2}{1 + (\lambda/l_i)^2}\right]^{\beta/2} \tag{3.1}$$

developed and tested by Thiesset *et al.* (2016) for exactly this purpose. The function smoothly connects the asymptotes $\mathcal{L} = \text{const.}$ for $\lambda \ll l_i$ and $\lambda \gg l_o$ (where $\mathcal{L}/L_x = 1$) with the fractal scaling $\mathcal{L}/L_x \propto (l_o/\lambda)^{\beta}$ for $l_i \lesssim \lambda \lesssim l_o$ in a way that closely agrees with the data, as can be inferred from the representative fit in figure 3. Results from applying (3.1) to the data are presented in figure 4(*a*–*f*). While, predominantly due to limited statistics, there is some scatter in figure 4(*a*,*c*,*e*) between individual time steps, the time-averaged trends are robust and allow for firm conclusions. Judging from the fact that $l_i/\hat{\eta}$ is approximately constant in time (cf. figure 4*a*) and indifferent to $\hat{Ri}_g$ (cf. figure 4*b*), it is concluded that $l_i \propto \hat{\eta}$, with $l_i \approx 10\hat{\eta}$. Similarly, figure 4(*c*,*d*) suggests that $l_o \propto \hat{h}$ and $l_o \approx 0.6$–$0.8\hat{h}$ for the GCs as well as the WJ. For the scaling exponent β in figure 4(*e*,*f*), however, significant differences appear. It is apparent – especially from the averages at late times in figure 4(*f*) – that β is a decreasing function of $\hat{Ri}_g$. For the WJ, β takes significantly longer than for the GCs to approach a constant value and, presumably due to confinement effects, never reaches the theoretically predicted value of $1/3$. The WJ grows fastest with the strongest interface contortions (see figures 1*a* and 2*a*) and is therefore most susceptible to interference due to the finite size of the computational domain. Based on the above results, $\mathcal{L}/L_x \propto (l_o/l_i)^{\beta} \propto (\hat{h}/\hat{\eta})^{\beta} \propto (Re^{3/4})^{\beta}$, and we note that β is the

https://doi.org/10.1017/jfm.2017.245 Published online by Cambridge University Press

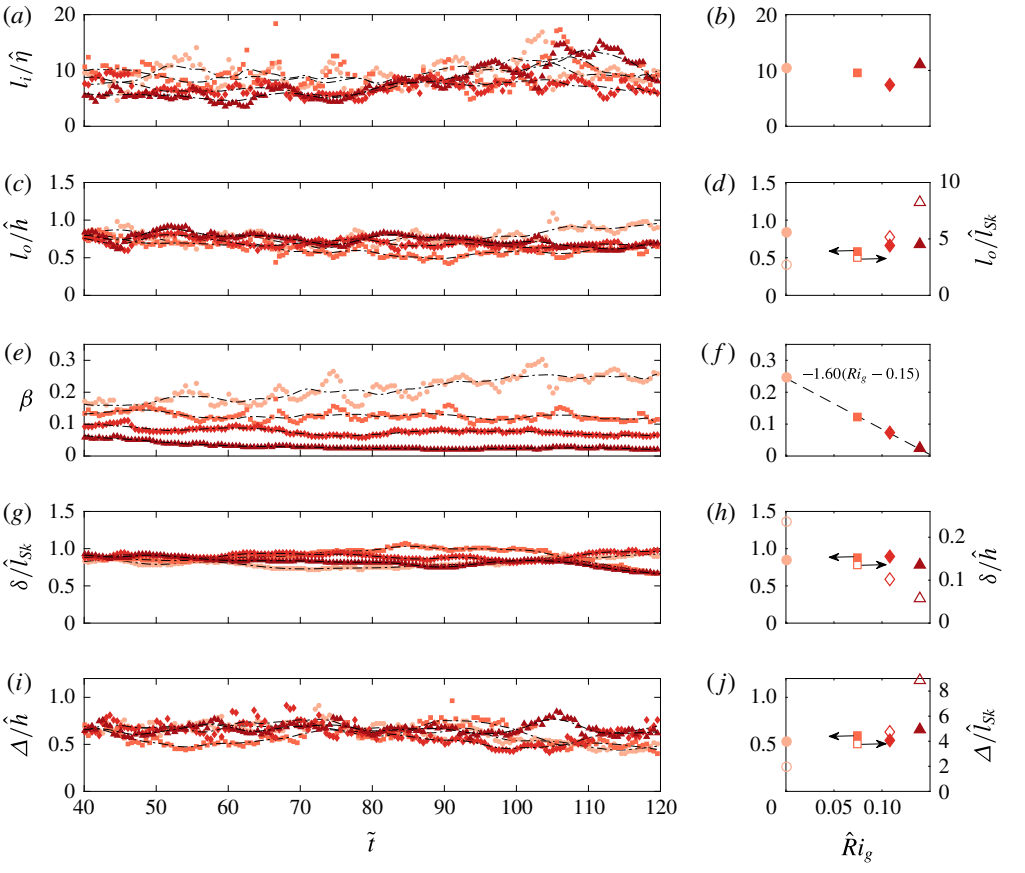


FIGURE 4. Results from applying the fit (3.1): inner cutoff $l_i/\hat{\eta}$ (*a*,*b*), outer cutoff $l_o/\hat{h}$ (*c*,*d*) and slope β (*e*,*f*), along with $\delta/\hat{l}_{Sk}$ (*g*,*h*) and $\Delta/\hat{h}$ (*i*,*j*), plotted as function of $\tilde{t}$ (*a*,*c*,*e*,*g*,*i*), with black lines indicating a moving average over $\approx 10\tilde{t}$, and of $\hat{Ri}_g$ averaged over $100 \leqslant \tilde{t} \leqslant 120$ (*b*,*d*,*f*,*h*,*j*). The legend from figure 3(*b*) applies; the open symbols in (*d*,*h*,*j*) relate to alternative normalizations on the right-hand axis. The dashed line in (*f*) represents a linear fit to the data with the parameters given in the figure.

decisive parameter in reducing $\mathcal{L}$ (or equivalently A_η). In fact, Re is larger for the GCs than for the WJ as the constant forcing $\sin\alpha B_0$ keeps increasing the volume flux $u_T h$. This also implies that the $\hat{Ri}_g$ trend of β cannot be an artefact of an increasingly restricted scaling range as it is in fact becoming slightly larger. Even though the linear fit in figure 4(*f*) appears suggestive, it lacks a physical underpinning. With the caveat that $\beta(\hat{Ri}_g = 0)$ is lower than the commonly accepted value of $\beta \approx 1/3$ in this case, it may however serve as an approximation at larger $\hat{Ri}_g$.

The observation that $l_o \propto \hat{h}$ might appear surprising, as one would expect the large-scale cutoff in stratified (or sheared) flows to be determined by a buoyancy (shear) scale. In fact, with $\hat{Ri}_g < 0.25$ (cf. figure 1*c*), all flows considered here are 'shear-dominated' according to the framework of Mater & Venayagamoorthy (2014). In this regime, the largest scales are of the order of the shear scale $\hat{l}_{Sk} = (\hat{k}^{1/2}/\hat{S})$, where k is the turbulent kinetic energy. However, from the open symbols in figure 4(*d*), it

https://doi.org/10.1017/jfm.2017.245 Published online by Cambridge University Press

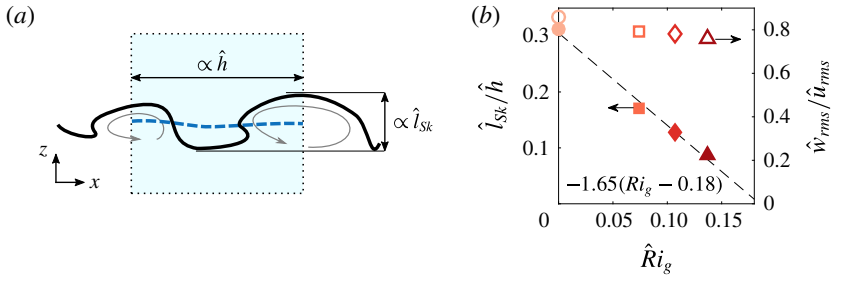


FIGURE 5. (*a*) Schematic of the anisotropic interface geometry. The shaded blue area represents a filter and the dashed blue line the filtered interface. (*b*) The ratio $\hat{l}_{Sk}/\hat{h}$ as a function of $\hat{Ri}_g$ (filled symbols) along with a linear fit to the data (dashed line and fit parameters). Also shown on the right-hand axis is the ratio of r.m.s. velocity fluctuations $\hat{w}_{rms}/\hat{u}_{rms}$ (open symbols).

becomes obvious that $\hat{l}_{Sk}$ is not the proper normalization for l_o. In addition to the fit results already discussed, the length scale δ, which characterizes the wall-normal fluctuations of the interface position z_i, is plotted in figure 4(*g*,*h*). It is defined by $\delta = \left[(1/\mathcal{L})\int (z_i(s) - \langle z_i \rangle)^2 \,\mathrm{d}s\right]^{1/2}$, with s denoting a curvilinear coordinate that runs along the TNTI. From the results in figure 4(*g*,*h*), there can be little doubt that $\delta(Ri_g)$ scales on $\hat{l}_{Sk}$ and not $\hat{h}$. In contrast, the scale Δ, which is designed to characterize the streamwise extent of interface convolutions by measuring the mean streamwise distance of the zero crossings of the function $z_i - \langle z_i \rangle$, is seen to scale on $\hat{h}$ (see figure 4*i*,*j*). Hence, there is an anisotropy in the scaling relations, the implications of which we will discuss in the following.

4. Discussion

The situation at the interface is sketched in figure 5(*a*). The different scalings of δ and Δ observed above suggest that eddies are distorted such that they produce convolutions whose size in x is approximately $\hat{h}$ but that are limited to $\hat{l}_{Sk}$ in z. The latter is consistent with the aforementioned shear cutoff and corresponds to the scaling expected in a homogeneous shear flow (Pope 2000). However, the finite extent of the shear layer, which is $\propto\hat{h}$, is seen to become relevant in the streamwise direction. This is consistent with the fact that the wavelength of the Kelvin–Helmholtz instability active here scales with the thickness of the shear layer (Schmid & Henningson 2000).

It is noteworthy that no comparable scaling anisotropy was detected in related studies on turbulent jets (Mistry *et al.* 2016) or boundary layers (e.g. Corrsin & Kistler 1954). In fact, this is not surprising since to a first approximation $l_{Sk} \propto l^*$ (where l^* is a transverse length scale of the jet or the boundary layer thickness) in these flows with no additional dependence on Ri.

With the above results, we have $\delta/\Delta \propto \hat{l}_{Sk}/\hat{h}$, which is smaller than 1 in all cases, as figure 5(*b*) shows. In this case, the filter width at which interface convolutions will be removed is set by their streamwise extent, as the sketch in figure 5(*a*) illustrates, which is consistent with $l_o \propto \hat{h}$ from figure 4(*c*,*d*). The results in figure 5(*b*) indicate that the anisotropy implied by the different scaling relations in different directions becomes more pronounced with increasing $\hat{Ri}_g$. We further note that from

https://doi.org/10.1017/jfm.2017.245 Published online by Cambridge University Press

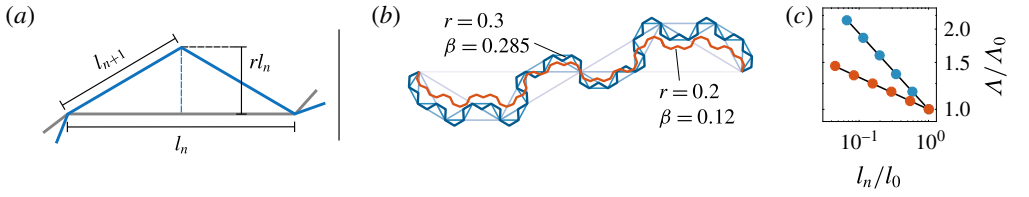


FIGURE 6. (*a*) Illustration of the construction of the model fractal. (*b*) Sample fractals after five iterations; darker shades of blue indicate increasing iterations for $r = 0.3$. (*c*) Normalized length Λ/Λ_0 for the two fractals (symbols) and predictions from (4.3) (lines).

the definition of $\hat{l}_{Sk}$, it follows that $\hat{l}_{Sk} = \hat{k}^{1/2}/S = \hat{k}^{1/2}/(\hat{u}/\hat{h}) = \hat{h}\hat{k}^{1/2}/\hat{u}$, such that the ratio plotted in figure 5(*b*) is equivalent to the turbulent intensity $\hat{k}^{1/2}/\hat{u}$. Also included in figure 5(*b*) is the ratio of root mean square (r.m.s.) velocity fluctuations in the wall-normal and streamwise directions. This ratio decreases much slower with $\hat{Ri}_g$ than $\hat{l}_{Sk}/\hat{h}$ or the turbulence intensity. Therefore, it follows that the decrease in $\hat{l}_{Sk}/\hat{h}$ is not predominantly related to increased anisotropy caused by the suppression of wall-normal velocity fluctuation due to the stable stratification. It is rather that – even as shear increases with increasing $\hat{Ri}_g$ (cf. the discussion of figure 1) – the flow becomes less efficient in producing turbulent fluctuations, resulting in lower turbulence intensities and thus lower $\hat{l}_{Sk}/\hat{h}$.

In the following, we will assess the effect of this disparity in length scales on the fractal slope β by replicating the geometry of the TNTI by a simple model fractal. The construction principle for the fractal curve is depicted in figure 6(*a*). At iteration n (represented by the grey line), the curve consists of N line segments with length l_n, such that its total length is $\Lambda_n = \Lambda(l_n) = Nl_n$. At the next iteration (blue line), a new point is introduced at a distance rl_n from the centre of l_n, where r is an anisotropy parameter, and it follows that

$$l_{n+1} = \left[\left(\frac{l_n}{2}\right)^2 + (rl_n)^2\right]^{1/2} = \frac{l_n}{2}m, \tag{4.1}$$

with the abbreviation $m = (1 + 4r^2)^{1/2}$. Alternating the side at which the new point is placed for consecutive line segments, as is done for the two sample fractals in figure 6(*b*), ensures that the mean position of the curve is preserved. With (4.1), we find that $\Lambda_{n+1} = 2Nl_{n+1} = Nl_n m$, and the fractal scaling from

$$\frac{\Lambda(l_{n+1})}{\Lambda(l_n)} = m = \left(\frac{l_n}{l_{n+1}}\right)^{\beta_m} = \left(\frac{2}{m}\right)^{\beta_m}, \tag{4.2}$$

with $\beta_m = f(m)$ denoting the fractal exponent of the model. Solving (4.2) for β_m yields

$$\beta_m = \frac{\ln m}{\ln \dfrac{2}{m}}, \tag{4.3}$$

which is also confirmed by the plot of Λ/Λ_0 versus l_n/l_0 in figure 6(*c*). From figure 6(*b*,*c*), it also becomes clear that lower values of r, i.e. stronger anisotropy, lead to lower fractal slopes β_m, similar to what has been observed in figure 4.

https://doi.org/10.1017/jfm.2017.245 Published online by Cambridge University Press

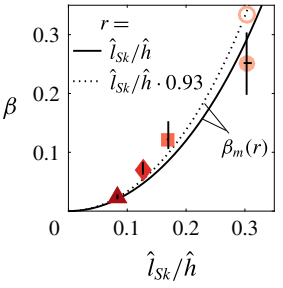


FIGURE 7. The slope β as a function of the ratio $\hat{l}_{Sk}/\hat{h}$ averaged over $100 < \tilde{t} < 120$ (filled symbols), with error bars indicating the full range of the data in that period. The open symbol marks the value of $\beta = 1/3$ for the unstratified case. The lines represent β_m according to (4.3) with $r = C\hat{l}_{Sk}/\hat{h}$ and different values of C.

If the decrease of β is in fact related to the increasing degree of anisotropy witnessed in figure 5(*b*), it should now be possible to find a proportionality constant $r = C\hat{l}_{Sk}/\hat{h}$ of order unity, such that $\beta(\hat{l}_{Sk}/\hat{h}) \approx \beta_m(r)$. Indeed, choosing $C = 1$ yields reasonable agreement between β and β_m, as evidenced by the plot in figure 7. We recall that β obtained from the present simulations for the WJ is lower than the established value of $\approx 1/3$, which is also included in figure 7. The correspondence between the data and the simple model is even better if this value is adopted along with $C = 0.93$.

It should be noted that in deriving the model in its present form, it was assumed that r, and hence the scaling anisotropy is independent of scale. Since results for both δ and l_o are dominated by the largest scales, this is not strictly implied by the data. As outlined in the discussion of figure 5(*b*), the anisotropy of the TNTI is not directly related to anisotropy in the velocity field. It is rather a consequence of the fact that the streamwise and wall-normal directions have different characteristic length scales. Hence, the assumption of scale invariance of r is not necessarily inconsistent with Kolmogorov's hypothesis of small-scale isotropy. For a definitive answer as to whether $r = \text{const.}$ is in fact applicable even when the scaling range is large, data at significantly higher Re would be required. In any case, a potential scaling transition can easily be accounted for in the model by rendering r a function of the scale, essentially resulting in a multifractal object.

Moreover, if $\beta \to 0$, then $A_\eta/A_0 \to 1$, and from (1.1) v_n is no longer amplified by interface convolutions. The local entrainment velocity is dominated by viscous processes at small thresholds (e.g. Holzner & Lüthi 2011), and hence entrainment reduces to pure diffusion in this limit such that $E \to 0$. Consistently, from extrapolating the direct measurements (figure 4*d*), as well as the model (figures 5*b* and 7), this limit is approached for $\hat{Ri}_g > 0.15$–0.18 in our data, which (from figure 1*c*) relates to $Ri \approx 0.2$. We note that this value is significantly lower than the value of 0.8 predicted by the fit based on experimental data by Turner (1986). Presumably this is related to non-equilibrium effects in the experiment, but we reserve a detailed discussion for a future publication in order to limit the scope of the present paper.

5. Concluding remarks

Recent studies link the reduction of entrainment with increasing stratification in gravity currents to a decrease of the surface area A_η of the TNTI. Here, we examined

https://doi.org/10.1017/jfm.2017.245 Published online by Cambridge University Press

the multiscale properties of this effect using DNS of flows in a range from unstratified to strongly stratified conditions characterized by the Richardson number $\hat{Ri}_g$. It was shown that the reduction of A_η with increasing $\hat{Ri}_g$ is linked to a decrease in the fractal scaling exponent β, while the inner and outer cutoffs of the scaling regime remain largely unaffected. Our results further show that interface convolutions scale differently in the streamwise and wall-normal directions. The former scales on the bulk scale $\hat{h}$ consistent with the underlying instability mechanism, while the latter scales on the shear scale $\hat{l}_{Sk}$, which is the large-scale cutoff in shear-dominated flows such as the present ones. This went unnoticed in previous studies since the two different scalings coincide in neutrally buoyant flows. The ratio $\hat{l}_{Sk}/\hat{h}$ and hence the anisotropy of the bulges were seen to decrease with increasing $\hat{Ri}_g$. It was finally found that a simple fractal model based on this finding convincingly predicts the dependence of β on $\hat{Ri}_g$. By allowing A_η to be parametrized in terms of basic turbulence quantities, these novel results may play an important role in modelling turbulent entrainment. Moreover, it appears likely that the present findings might – at least in part – also transfer to other problems such as the deepening of the wind-mixed layer (Pollard, Rhines & Thompson 1972).

References

Corrsin, S. & Kistler, A. 1954 The free-stream boundaries of turbulent flows. *NACA* TN-3133, TR-1244, 1033–1064.

Craske, J. & van Reeuwijk, M. 2015 Energy dispersion in turbulent jets. Part 1. Direct simulation of steady and unsteady jets. *J. Fluid Mech.* **763**, 500–537.

Da Silva, C. B., Hunt, J. C. R., Eames, I. & Westerweel, J. 2014 Interfacial layers between regions of different turbulence intensity. *Annu. Rev. Fluid Mech.* **46**, 567–590.

Dimotakis, P. E. & Catrakis, H. J. 1999 Turbulence, fractals, and mixing. In *Mixing: Chaos and Turbulence* (ed. H. Chaté, E. Villermaux & J.-M. Chomaz), pp. 59–143. Springer.

Ellison, T. H. & Turner, J. S. 1959 Turbulent entrainment in stratified flows. *J. Fluid Mech.* **6** (03), 423–448.

Holzner, M. & Lüthi, B. 2011 Laminar superlayer at the turbulence boundary. *Phys. Rev. Lett.* **106** (13), 134503.

Kneller, B., Nasr-Azadani, M. M., Radhakrishnan, S. & Meiburg, E. 2016 Long-range sediment transport in the world's oceans by stably stratified turbidity currents. *J. Geophys. Res. Oceans* **121**, 8608–8620.

Krug, D., Holzner, M., Lüthi, B., Wolf, M., Kinzelbach, W. & Tsinober, A. 2015 The turbulent/non-turbulent interface in an inclined dense gravity current. *J. Fluid Mech.* **765**, 303–324.

Mandelbrot, B. B. 1982 *The Fractal Geometry of Nature*. W.H. Freeman.

Mater, P. D. & Venayagamoorthy, S. K. 2014 A unifying framework for parameterizing stably stratified shear-flow turbulence. *Phys. Fluids* **26** (3), 036601.

Mistry, D., Philip, J., Dawson, J. R. & Marusic, I. 2016 Entrainment at multi-scales across the turbulent/non-turbulent interface in an axisymmetric jet. *J. Fluid Mech.* **802**, 690–725.

Paizis, S. T. & Schwarz, W. H. 1974 An investigation of the topography and motion of the turbulent interface. *J. Fluid Mech.* **63** (02), 315–343.

Pollard, R. T., Rhines, P. B. & Thompson, R. O. R. Y. 1972 The deepening of the wind-mixed layer. *Geophys. Astrophys. Fluid Dyn.* **4** (1), 381–404.

Pope, S. B. 2000 *Turbulent Flows*. Cambridge University Press.

van Reeuwijk, M. & Holzner, M. 2014 The turbulence boundary of a temporal jet. *J. Fluid Mech.* **739**, 254–275.

van Reeuwijk, M., Krug, D. & Holzner, M. 2017 Small-scale entrainment in inclined gravity currents. *Environ. Fluid Mech.* doi:10.1007/s10652-017-9514-3.

https://doi.org/10.1017/jfm.2017.245 Published online by Cambridge University Press

SCHMID, P. J. & HENNINGSON, D. S. 2000 *Stability and Transition in Shear Flows*. Springer.

SEQUEIROS, O. E. 2012 Estimating turbidity current conditions from channel morphology: a Froude number approach. *J. Geophys. Res.* **117**, C04003.

SEQUEIROS, O. E., SPINEWINE, B., BEAUBOUEF, R. T., SUN, T., GARCÍA, M. H. & PARKER, G. 2010 Characteristics of velocity and excess density profiles of saline underflows and turbidity currents flowing over a mobile bed. *J. Hydraul. Engng ASCE* **136** (7), 412–433.

DE SILVA, C. M., PHILIP, J., CHAUHAN, K., MENEVEAU, C. & MARUSIC, I. 2013 Multiscale geometry and scaling of the turbulent–nonturbulent interface in high Reynolds number boundary layers. *Phys. Rev. Lett.* **111**, 044501.

SREENIVASAN, K. R. 1991 Fractals and multifractals in fluid turbulence. *Annu. Rev. Fluid Mech.* **23** (1), 539–604.

SREENIVASAN, K. R., RAMSHANKAR, R. & MENEVEAU, C. 1989 Mixing, entrainment and fractal dimensions of surfaces in turbulent flows. *Proc. R. Soc. Lond.* A **421** (1860), 79–108.

THIESSET, F., MAURICE, G., HALTER, F., MAZELLIER, N., CHAUVEAU, C. & GÖKALP, I. 2016 Geometrical properties of turbulent premixed flames and other corrugated interfaces. *Phys. Rev.* E **93** (1), 013116.

TURNER, J. S. 1986 Turbulent entrainment – the development of the entrainment assumption, and its application to geophysical flows. *J. Fluid Mech.* **173**, 431–471.

https://doi.org/10.1017/jfm.2017.245 Published online by Cambridge University Press